

Sparse Regularization-Based Fuzzy C-Means Clustering Incorporating Morphological Grayscale Reconstruction and Wavelet Frames

Cong Wang, Witold Pedrycz, *Fellow, IEEE*, MengChu Zhou, *Fellow, IEEE*, and ZhiWu Li, *Fellow, IEEE*

Abstract—The conventional Fuzzy *C*-Means (FCM) algorithm is not robust to noise and its rate of convergence is generally impacted by data distribution. Consequently, it is challenging to develop FCM-related algorithms that have good performance and require less time. In this paper, we elaborate on a comprehensive FCM-related algorithm for image segmentation. To make FCM robust, we first utilize a morphological grayscale reconstruction (MGR) operation to filter observed images before clustering, which guarantees noise-immunity and image detail-preservation. Since real images can generally be approximated by sparse coefficients in tight wavelet frame systems, feature spaces of observed and filtered images can be obtained. Taking such features to be clustered, we investigate an improved FCM model in which a sparse regularization term is introduced into the objective function of FCM. We design a three-step iterative algorithm to solve the sparse regularization-based FCM model, which is constructed by the Lagrangian multiplier method, hard-threshold operator, and normalization operator, respectively. Such an algorithm can not only perform well for image segmentation, but also comes with high computational efficiency. To further enhance the segmentation accuracy, we use MGR to filter the label set generated by clustering. Finally, a large number of supporting experiments and comparative studies with other FCM-related algorithms available in the literature are provided. The obtained results for synthetic, medical and color images indicate that the proposed algorithm has good ability for multiphase image segmentation, and performs better than other alternative FCM-related algorithms. Moreover, the proposed algorithm requires less time than most of the existing algorithms.

Index Terms—Fuzzy *C*-Means algorithm; image segmentation; sparse regularization; morphological grayscale reconstruction; tight wavelet frame.

This work was supported in part by the Doctoral Students' Short Term Study Abroad Scholarship Fund of Xidian University, in part by the National Natural Science Foundation of China under Grant Nos. 61873342, 61672400, in part by the Recruitment Program of Global Experts, and in part by the Science and Technology Development Fund, MSAR, under Grant No. 0012/2019/A1. (*Corresponding author: MengChu Zhou and ZhiWu Li*)

C. Wang is with the School of Electro-Mechanical Engineering, Xidian University, Xi'an 710071, China (e-mail: wangle0705@stu.xidian.edu.cn).

W. Pedrycz is with the Department of Electrical and Computer Engineering, University of Alberta, Edmonton, AB T6R 2V4, Canada, the School of Electro-Mechanical Engineering, Xidian University, Xi'an 710071, China, and also with the Faculty of Engineering, King Abdulaziz University, Jeddah 21589, Saudi Arabia (e-mail: wpedrycz@ualberta.ca).

M. Zhou is with the Institute of Systems Engineering, Macau University of Science and Technology, Macau 999078, China and also with the Helen and John C. Hartmann Department of Electrical and Computer Engineering, New Jersey Institute of Technology, Newark, NJ 07102 USA (e-mail: zhou@njit.edu).

Z. Li is with the School of Electro-Mechanical Engineering, Xidian University, Xi'an 710071, China, and also with the Institute of Systems Engineering, Macau University of Science and Technology, Macau, China (e-mail: zhwl@xidian.edu.cn).

I. INTRODUCTION

IMAGE segmentation, as a fundamental image operation, aims to divide an image into several non-overlapped and consistent regions. It is often a challenging task in computer vision and image understanding. Over the past three decades, a series of image segmentation technologies were proposed [1]–[10], [14], [15]. Such technologies involve various unsupervised or supervised approaches, such as clustering [1]–[4], watershed transform [5], Graph Cut [6], neural network [7]–[9], and active contour model [10]. Among them, clustering is widely applied to image segmentation due to its effectiveness, thus resulting in a large number of clustering-based algorithms [11]–[19]. Generally speaking, traditional clustering-based algorithms are usually Boolean (binary) in the sense that they admit pixels to exclusively belong to a single cluster. Whereas, superior to these algorithms, a Fuzzy *C*-Means (FCM) algorithm is soft in its nature since it assigns image pixels to multiple clusters based on a collection of degrees of membership assuming values in the unit interval. However, the conventional FCM algorithm is of sensitiveness to noise and its rate of convergence is generally impacted by data distribution characteristics. Consequently, FCM-related algorithms that can remove noise and require less time simultaneously are not well exploited.

To address this challenging problem, we innovatively propose a sparse regularization-based FCM algorithm for image segmentation through incorporating morphological grayscale reconstruction (MGR) [20], [21] and a tight wavelet frame transform [22], [23]. The framework of the proposed algorithm is illustrated in Fig. 1. In order to improve the robustness of the FCM, we first use MGR to filter observed images. A tight wavelet frame system is utilized to acquire feature spaces of observed and filtered images, i.e., high- and low-frequency information. Taking these feature sets as data of clustering, an improved FCM algorithm is presented for segmenting feature sets where a sparse regularization term is introduced into the objective function of FCM. To further reduce the misclassification rate, we use MGR to filter labels generated by clustering, which makes segmentation accuracy improved as much as possible. Finally, by combining the prototypes and filtered label set, segmented images are reconstructed by the tight wavelet frame reconstruction operation.

This paper offers four main contributions to the advancement of the area. First, to improve simultaneously noise-immunity and retention capacity of image details, we employ

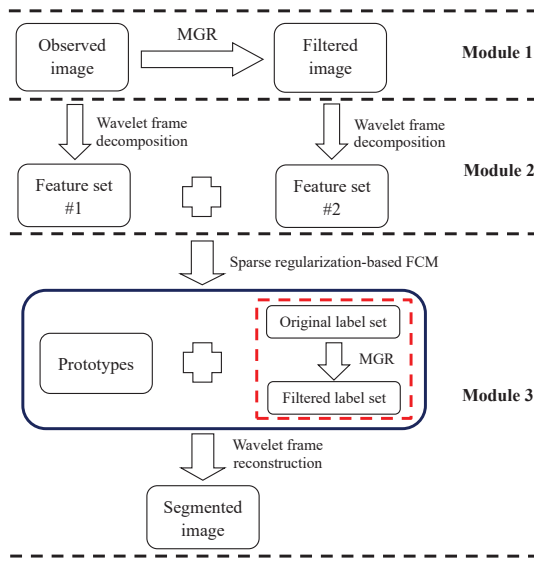


Fig. 1. The framework of the proposed algorithm.

MGR to filter images for the further segmentation. This means that MGR introduces spatial information of images into the objective function of FCM. Therefore, the usage of MGR makes FCM more robust to different types of noise.

The second contribution is that a tight wavelet frame system is borrowed to form feature sets of images, which removes the difficulty of the direct use of image pixels. Since real images can be approximated by sparse coefficients in tight wavelet frame systems, information in images can be sufficiently analyzed and manipulated. The underlying idea of using the wavelet frame system is to transform original data space to a new feature space. The new feature space is advantageous for analyzing and manipulating image data and further makes underlying image features and noise easy to find.

The third contribution is to bring a sparse regularization term into the objective function of FCM, thus forming a sparse regularization-based FCM model. This term constrains the redundancy of degrees of membership, thus leading to the strong sparsity of the partition matrix generated by FCM. For each iteration of FCM, all degrees of membership of each pixel with respect to all clusters do not have to be calculated since they lead to a low rate of convergence of FCM. Hence, sparse regularization greatly improves the computational efficiency of FCM. Furthermore, the segmentation accuracy of FCM is also improved to some extent.

Finally, we make a contribution by designing a three-step iterative algorithm to solve the sparse regularization-based FCM model. The proposed algorithm is constructed by the Lagrangian multiplier method, hard-threshold operator, and normalization operator, respectively. In particular, we apply the Lagrangian multiplier method to achieve the exact solution to the first inner problem of the proposed algorithm.

Except for four main contributions mentioned above, we also prudently use MGR to filter labels generated by clustering, which reduces the possibility of misclassification. Clearly, this step is also a non-overlooked contribution of the proposed algorithm.

The paper is organized as follows. Section II reviews some related works on FCM, and makes some comments. Section III briefly formulates FCM and a wavelet frame transform. Section IV introduces the proposed algorithm step by step. In Section V, experimental results for synthetic, medical and color images are reported. Conclusions are reached in Section VI.

II. RELATED WORKS

In this section, FCM-related image segmentation techniques are briefly reviewed. The FCM algorithm was first introduced by Dunn [1], and further improved by Bezdek [2]. Since the conventional FCM algorithm is sensitive to noise, non-robust results are usually acquired. To deal with this problem, researchers mainly focused on two directions: considering spatial information of images [15], [16], [24]–[26] and using kernel distances [14], [17], [27]–[29].

In light of the first investigation, a number of improved FCM algorithms have been presented [15], [16], [24]–[26]. For example, Ahmed et al. [15] propose an improved FCM algorithm, namely FCM_S, by introducing spatial information into the objective function of FCM. FCM_S has to compute a spatial neighbors term for each iteration. Although FCM_S makes full use of impact of neighboring pixels, it has high computational complexity. In order to overcome the drawback of FCM_S, Chen and Zhang [16] utilize average and median filters to preprocess observed images in advance. Thus two variants of FCM_S, FCM_S1 and FCM_S2, with a higher computational efficiency than FCM_S are proposed. However, they do not work well for Gaussian or other well-known noise since prior knowledge of noise cannot be ascertained. Subsequently, Szilagyi et al. [24] introduce an enhanced FCM algorithm (EnFCM) by considering a summed image as data of FCM. EnFCM is time-saving since it executes clustering depending on gray level histograms instead of pixels. However, the segmentation results of EnFCM are only superior to those of FCM_S. For improving EnFCM's results, Cai et al. [25] propose a fast generalized FCM algorithm (FGFCM) by incorporating a local similarity measure. Similar to EnFCM, this algorithm requires less computational time due to the usage of gray level histograms. However, it requires more parameters to balance robustness to noise and effect of retaining feature details. In general, the parameter selection within FGFCM depends on experience and trial-and-error. In order to simplify the parameter setting of FGFCM, Krnidis et al. [26] report a novel algorithm, namely FLICM, by using a fuzzy factor to replace parameters in FGFCM. Compared with FGFCM, FLICM is not only free of parameter setting, but also improves the segmentation effect. However, the drawback of FLICM comes with the usage of the non-robust Euclidean distance that is not effective for arbitrary spatial information of images.

To overcome FLICM's shortcoming, another investigation is to introduce robust kernel distances into its objective function. The aim of kernel distances is to transform the original data space to a new feature space by using a nonlinear mapping. Hence, the essence of target data can be easily found and manipulated. The wide usage of kernel distances leads to

a series of kernel-based FCM algorithms [14], [17], [27]–[29]. For instance, Gong et al. [17] propose an improved FCM algorithm (KWFLICM) based on a tradeoff weighted fuzzy factor and a kernel metric. KWFLICM improves the robustness of FLICM to different types of noise, and does not require any parameter setting. Nevertheless, it is more time-consuming than FLICM. Zhao et al. [27] report a neighborhood weighted FCM algorithm (NWFCM). It defines a neighborhood weighted-distance to replace a usual Euclidean distance in FCM. Although NWFCM requires less time than FLICM and KWFLICM, its computational efficiency is still lower than most FCM-related algorithms because of using the patch distance and setting parameters. Elazab et al. [28] present an FCM framework (ARKFCM) that incorporates the Gaussian radial basis kernel function into the objective function of FCM. This framework performs well for fixed noise, but is not robust when coping with unknown noise. Recently, Wang et al. [14] propose a wavelet frame-based FCM algorithm (WFCM) and apply it to segment images in non-flat domains. This algorithm considers wavelet frames as a kernel function, thus forming feature spaces of images. Compared with other existing algorithms, WFCM has a better capability to recognize image features.

In addition, many comprehensive FCM-related algorithms involving in various mathematical techniques, such as Kullback-Leibler (KL) divergence, morphological reconstruction, and sparse representation, have been recently proposed [18], [19], [30], [31].

For example, Gharieb et al. [30] employ the KL divergence to modify the objective function of the *C*-Means algorithm, thus forming a developed FCM algorithm. This algorithm works well on the basis of local membership and locally-smoothed data. However, it is time-consuming due to the usage of local information for each iteration. Gu et al. [18] present a fuzzy double *C*-Means algorithm (FDCM) by introducing sparse representation into FCM. Differing other FCM-related algorithms, FDCM can address two datasets simultaneously. The one is the basic feature set obtained from original images. The other is a learning feature set coming from a spare self-representation model. FDCM is robust to noise, thus it has good clustering performance. However, it has higher computational complexity than other algorithms. More recently, Lei et al. [19] propose a fast and robust FCM algorithm (FRFCM) by incorporating MGR and membership filtering, which are regarded as pre- and post-processing steps in addition to the main clustering algorithm. FRFCM performs clustering on the basis of gray level histograms, thus it is fast. However, its performance can still be improved.

Through reviewing the related work, it is concluded that existing algorithms pay much attention to segmentation effect or computational efficiency, but cannot simultaneously take them into consideration. Even though these algorithms are effective for image segmentation, their computational efficiency is usually low due to multiple factors, such as parameter selection, high-dimensional data space, and image patch. In addition, we also find that existing algorithms in the literature mostly depend on the improvement of non-Euclidean distance and noise detection to low the computational complexity. Es-

pecially, they ignore discussion on the sparsity of the partition (membership) matrix generated by clustering. Consequently, FCM-related algorithms that have simultaneously good performance and require less time are not well exploited.

Inspired by recent work in [14], [19], we propose a comprehensive FCM-related algorithm. One of our motivations is to use MGR to filter images before segmentation, which means that spatial information of images is introduced into FCM. What's more, we innovatively employ a wavelet frame system to transform image pixels to feature spaces of images, which makes information in images sufficiently analyzed and manipulated. The proposed algorithm can naturally be regarded as a kernel-based FCM algorithm when taking tight wavelet frames as a kernel function.

Under the premise of ensuring good segmentation performance, we also do our best to reduce the computational time. For each iteration of FCM, degrees of membership of each pixel with respect to all clusters have to be calculated. Thus it leads to a low rate of convergence. Actually, the calculation of all degrees of membership is redundant. However, if pixels are only assigned to a single cluster, FCM reduces to *K*-Means. Therefore, we can guarantee that the partition matrix has a certain sparsity in order to reduce the iteration count of FCM. In light of this point, we introduce a sparse regularization term about degrees of membership into the objective function of FCM. It greatly enhances the computational efficiency of clustering.

In addition, the rate of convergence of FCM is generally determined by data distributions. Thus, the usage of MGR and a tight wavelet frame system before clustering makes distribution characteristics of image pixels adaptive to fuzzy clustering. It also reduces the computational cost of clustering. In conclusion, the proposed algorithm has good performance for image segmentation with high computational efficiency.

III. PRELIMINARIES

A. FCM Algorithm

Given is a gray image f of size $M \times N$. We express it as a K -dimensional vector, where K represents the number of image pixels, i.e., $K = M \times N$. Due to various underlying attributes (variables) of pixels, we can formulate f as data $\mathbf{X} = \{\mathbf{x}_1, \mathbf{x}_2, \dots, \mathbf{x}_K\} \subset \mathbb{R}^K$. The FCM algorithm divides \mathbf{X} into several clusters. Its objective function is

$$J = \sum_{i=1}^c \sum_{j=1}^K u_{ij}^m \|\mathbf{x}_j - \mathbf{v}_i\|^2,$$

where $\mathbf{U} = [u_{ij}]_{c \times K}$ is a partition (membership) matrix with a constraint of $\sum_{i=1}^c u_{ij} = 1$ and $0 \leq u_{ij} \leq 1$, m is the fuzziness coefficient ($m > 1$), $\|\cdot\|$ denotes the Euclidean distance, and c is the number of clusters.

The iterative updates of the partition matrix and prototypes are given as follows [32]:

$$u_{ij} = \frac{(\|\mathbf{x}_j - \mathbf{v}_i\|^2)^{-\frac{1}{m-1}}}{\sum_{q=1}^c (\|\mathbf{x}_j - \mathbf{v}_q\|^2)^{-\frac{1}{m-1}}} \quad \text{and} \quad \mathbf{v}_i = \frac{\sum_{j=1}^K u_{ij}^m \mathbf{x}_j}{\sum_{j=1}^K u_{ij}^m}.$$

This iterative updates of the partition matrix and prototypes stop when the termination condition $\|U^{(t)} - U^{(t-1)}\| < \epsilon$ has been met, where ϵ is a nonnegative threshold, and t denotes an iteration index of FCM.

B. Tight Wavelet frame Transform

Wavelet frames have a powerful ability to provide redundant representations of images. Over the past two decades, wavelet frames have been applied to a variety of applications, such as image segmentation [14], [33], [34], image restoration [23], [35], image denoising [36], [37], and surface reconstruction [38], [39]. In this subsection, we briefly describe the main idea of a tight wavelet frame transform. More details can be found in [22], [23]. The discrete wavelet frame decomposition, denoted as \mathcal{W} , can be generated by collecting all filters (masks) in a wavelet frame system. The linear operator (matrix) \mathcal{W} consists of γ sub-filtering operators, i.e., $\mathcal{W}_0, \mathcal{W}_1, \dots, \mathcal{W}_{\gamma-1}$. Among them, \mathcal{W}_0 is a low-pass filtering operator and the rest are high-pass filtering operators. According to unitary extension principle [40], the tight wavelet frame reconstruction, denoted as \mathcal{W}^T , can be obtained. Thus, we have $\mathcal{W}^T \mathcal{W} f = f$, where $\mathcal{W}^T \mathcal{W}$ is an identity operation, and f is a gray image.

IV. METHODOLOGY

A. Image Pixel Filtering via MGR

MGR has good performance for preserving object contours and removing noise simultaneously. Before applying FCM, we introduce MGR to filter images for the achievement of optimal distribution characteristic of image pixels.

Formally speaking, MGR contains two basic operators, i.e., dilation and erosion reconstructions [41]. Given two images f (mask image) and g (marker image), we denote the dilation reconstruction as $\mathcal{R}_f^D(g)$ that is formulated by

$$\mathcal{R}_f^D(g) = \mathcal{D}^{(t)}(g),$$

where $\mathcal{D}_f^{(t)}(g)$ is defined as

$$\mathcal{D}_f^{(t)}(g) = \begin{cases} \mathcal{D}(g) \wedge f, & t = 1 \\ \mathcal{D}(\mathcal{D}^{(t-1)}(g)) \wedge f, & t = 2, 3, \dots \end{cases}$$

where $g \leq f$, \wedge stands for the point-wise minimum and \mathcal{D} represents the dilation of g by a flat structuring element [21].

The erosion reconstruction is denoted by $\mathcal{R}_f^E(g)$:

$$\mathcal{R}_f^E(g) = \mathcal{E}_f^{(t)}(g),$$

where $\mathcal{E}_f^{(t)}(g)$ is defined as

$$\mathcal{E}_f^{(t)}(g) = \begin{cases} \mathcal{E}(g) \vee f, & t = 1 \\ \mathcal{E}(\mathcal{E}^{(t-1)}(g)) \vee f, & t = 2, 3, \dots \end{cases}$$

where $g \geq f$, \vee stands for the point-wise maximum and \mathcal{E} represents the erosion of g by a flat structuring element.

At the beginning of MGR, we have to select marker and mask images. The observed image is generally considered as a mask image, then its transformation is used as a marker image. For real applications, $g = \mathcal{E}(f)$ and $g = \mathcal{D}(f)$ are selected as marker images for dilation and erosion reconstructions, respectively.

On the basis of dilation and erosion reconstructions, the morphological closing reconstruction of f is defined as

$$\mathcal{R}^C(f) = \mathcal{R}_{\mathcal{R}_f^D(\mathcal{E}(f))}^E(\mathcal{D}(\mathcal{R}_f^D(\mathcal{E}(f)))). \quad (1)$$

Here, let \bar{f} be the filtered image, i.e., $\bar{f} = \mathcal{R}^C(f)$.

In order to show the filtering effect of MGR in presence of different types of noise, we show an example in Fig. 2. Here, we take a square of size 3×3 as the structuring element.

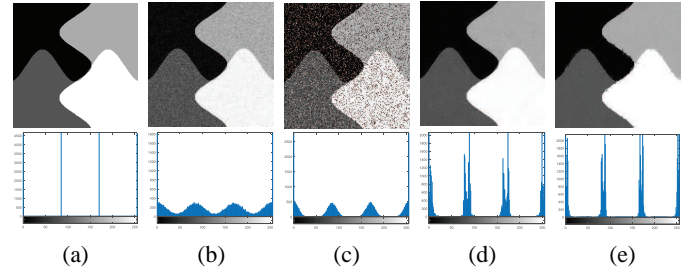


Fig. 2. Filtered results using MGR. (a) Original image; (b) image corrupted by AWGN ($s = 20$); (c) image corrupted by mixed Gaussian and impulse noise ($s = 10, r = 20\%$); (d) filtered result for (b); (e) filtered result for (c).

As shown in Fig. 2, there exist four obvious peaks in the gray level histogram of the original image. However, gray level histograms of images contaminated by additive white Gaussian noise (AWGN, with standard deviation s) or a mixture of AWGN and salt and pepper impulse noise (SPIN, with density r) have no obvious peaks except extremums (0 and 255). In Figs. 2(d)–(e), pixels of filtered images are usually split into 4 clusters. The results are similar to those of Fig. 2(a). Thus, MGR can effectively retain object contours and remove noise.

To achieve better segmentation, we integrate MGR into FCM. We still take Fig. 2 as an example. TABLE I shows the comparison between noisy and filtered images about iterations of FCM in presence of different types of noise. Here, we set $c = 4$.

TABLE I
COMPARISON BETWEEN NOISY AND FILTERED IMAGES ABOUT
ITERATIONS OF FCM

Noise level	Noisy image	Filtered image
$s = 20$	16	10
$r = 20\%$	11	8

TABLE I indicates that the number of iterations of FCM on filtered images is lower than that on noisy images. As the number of iterations decreases, MGR is effective for optimizing data distribution.

B. Feature Extraction via Wavelet Frames

Since the piecewise linear B-spline tight frame system [40], [42] can redundantly represent images, it has more adaptive properties to noise. Hence, we adopt this system. Formally speaking, the corresponding filters in discrete version are

$$a_0 = \left[\frac{1}{4}, \frac{1}{2}, \frac{1}{4} \right], a_1 = \left[-\frac{1}{4}, \frac{1}{2}, -\frac{1}{4} \right], a_2 = \left[\frac{\sqrt{2}}{4}, 0, -\frac{\sqrt{2}}{4} \right].$$

The above one-dimensional filters are able to generate nine two-dimensional filters, including a single low-pass filter and eight high-pass filters, corresponding to nine tight wavelet frame operators $\mathcal{W}_0, \mathcal{W}_1, \dots, \mathcal{W}_8$. Thus, we can employ tight wavelet frames to generate feature spaces of images, i.e., $\mathbf{X} = \mathcal{W}f$ and $\overline{\mathbf{X}} = \mathcal{W}\overline{f}$, where \mathbf{X} is the feature set associated with image f , $\overline{\mathbf{X}}$ is that with filtered image \overline{f} . Here, \mathcal{W}_0f and $\mathcal{W}_0\overline{f}$ represent low-frequency information, and the rest are high-frequency information. In order to exhibit the effect of wavelet frames, an example is shown in Fig. 3.

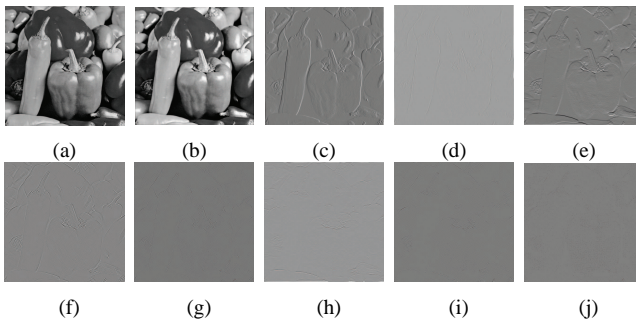


Fig. 3. Original image f and its wavelet coefficients. (a) Original image f ; (b)–(j) $\mathcal{W}_0f, \mathcal{W}_1f, \dots, \mathcal{W}_8f$.

Fig. 3(b) represents low-frequency information in image f . Moreover, Figs. 3(c)–(j) represent high-frequency information in image f . Clearly, tight wavelet frame systems can redundantly represent images, thus they offer more adaptive properties to feature details.

C. Sparse Regularization-Based FCM

Under the premise of ensuring good segmentation performance, we also try to enhance the computational efficiency. We can guarantee that the partition matrix has a certain sparsity to reduce the iteration count of FCM. Therefore, we introduce a sparse regularization term about degrees of membership. The detailed formulation is described as follows.

To implement clustering, we reformulate $\mathbf{X} = \mathcal{W}f = \{\mathbf{x}_1, \mathbf{x}_2, \dots, \mathbf{x}_K\}$ and $\overline{\mathbf{X}} = \mathcal{W}\overline{f} = \{\overline{\mathbf{x}}_1, \overline{\mathbf{x}}_2, \dots, \overline{\mathbf{x}}_K\}$, which denote sets of feature vectors associated with f and \overline{f} . To optimize the rate of convergence of clustering, we introduce the sparse ℓ_0 -norm regularization into the objective function of FCM. The modified objective function is represented as follows:

$$J = \sum_{i=1}^c \sum_{j=1}^K u_{ij}^m (\|\mathbf{x}_j - \mathbf{v}_i\|^2 + \alpha \|\overline{\mathbf{x}}_j - \mathbf{v}_i\|^2) + \beta \|\mathbf{U}\|_{\ell_0}, \quad (2)$$

where α and β are positive numbers that control the impacts of filtered term $\|\overline{\mathbf{x}}_j - \mathbf{v}_i\|^2$ and sparse regularization term $\|\mathbf{U}\|_{\ell_0}$ respectively. $\|\cdot\|_{\ell_0}$ denotes the ℓ_0 vector norm. For example, $\|\mathbf{U}\|_{\ell_0}$ is defined to be the number of nonzero entries in \mathbf{U} , which is formulated as

$$\|\mathbf{U}\|_{\ell_0} = \sum_{i=1}^c \sum_{j=1}^K |u_{ij}|_0$$

with

$$|u_{ij}|_0 = \begin{cases} 1, & u_{ij} \neq 0 \\ 0, & u_{ij} = 0 \end{cases}.$$

We design an optimization framework to minimize (2):

Step 1: Solve $\boldsymbol{\eta}, \mathbf{V}$.

$$\begin{aligned} (\boldsymbol{\eta}, \mathbf{V}) = \arg \min & \sum_{i=1}^c \sum_{j=1}^K \eta_{ij}^m (\|\mathbf{x}_j - \mathbf{v}_i\|^2 + \alpha \|\overline{\mathbf{x}}_j - \mathbf{v}_i\|^2) \\ \text{s.t. } & \sum_{i=1}^c \eta_{ij} = 1, \text{ for } j = 1, 2, \dots, K \end{aligned}, \quad (3)$$

where $\boldsymbol{\eta} = [\eta_{ij}]_{c \times K}$ and $\mathbf{V} = \{\mathbf{v}_i\}_{i=1,2,\dots,c}$.

Step 2: Solve $\tilde{\mathbf{U}}$.

$$\tilde{\mathbf{U}} = \mathcal{T}_\beta(\boldsymbol{\eta}), \quad (4)$$

where \mathcal{T} is a hard-threshold operator and $\mathcal{T}_\beta(\boldsymbol{\eta})$ is defined as:

$$\mathcal{T}_\beta(\boldsymbol{\eta}) = [\mathcal{T}_\beta(\eta_{ij})]_{c \times K}$$

with

$$\mathcal{T}_\beta(\eta_{ij}) := \begin{cases} \eta_{ij}, & \eta_{ij} \geq \sqrt{\beta} \\ 0, & \eta_{ij} < \sqrt{\beta} \end{cases}.$$

Moreover, $0 < \sqrt{\beta} \leq \min_{j=1,2,\dots,K} \{ \max_{i=1,2,\dots,c} [\eta_{ij}] \}$.

Step 3: Solve \mathbf{U} .

$$\mathbf{U} = \text{normalize}(\tilde{\mathbf{U}}), \quad (5)$$

with element $u_{ij} = \tilde{u}_{ij} / \sum_{i=1}^c \tilde{u}_{ij}$. Here, normalize denotes a normalization operator.

Obviously, there exist three steps in the framework. η_{ij} is first obtained by solving (3). Then we apply a hard-threshold operator to η_{ij} , thus generating \tilde{u}_{ij} . Finally, u_{ij} is acquired by imposing a normalization operator on \tilde{u}_{ij} , which is an optimal approximation solution to (2). In **Step 1**, η_{ij} is an exact solution to (3) and just a transitional value of u_{ij} , which means that η_{ij} is a rough fuzzy membership without sparsity. We can acquire η_{ij} by the assistance of Lemma IV.1. The details are reached as follows.

Lemma IV.1. Consider the minimization problem (3). By applying the Lagrangian multiplier method to solve (3), its iterative solutions are obtained as follows:

$$\eta_{ij} = \frac{(\|\mathbf{x}_j - \mathbf{v}_i\|^2 + \alpha \|\overline{\mathbf{x}}_j - \mathbf{v}_i\|^2)^{-\frac{1}{m-1}}}{\sum_{q=1}^c (\|\mathbf{x}_j - \mathbf{v}_q\|^2 + \alpha \|\overline{\mathbf{x}}_j - \mathbf{v}_q\|^2)^{-\frac{1}{m-1}}}, \quad (6)$$

$$\mathbf{v}_i = \frac{\sum_{j=1}^K \eta_{ij}^m (\mathbf{x}_j + \alpha \overline{\mathbf{x}}_j)}{(1 + \alpha) \sum_{j=1}^K \eta_{ij}^m}. \quad (7)$$

Proof. See the Appendix. \square

We here test two examples (refer to Figs. 4 and 5) to demonstrate the impact of the sparse ℓ_0 -norm regularization on the FCM. Fig. 4 shows how the sparse ℓ_0 -norm regularization optimizes the membership partition. In order to better express the performance optimization, we consider the image filtering and set $\alpha = 2$. As shown in Fig. 4, when $\beta = 0.01$, the sparse ℓ_0 -norm regularization makes the proper membership partition stronger.

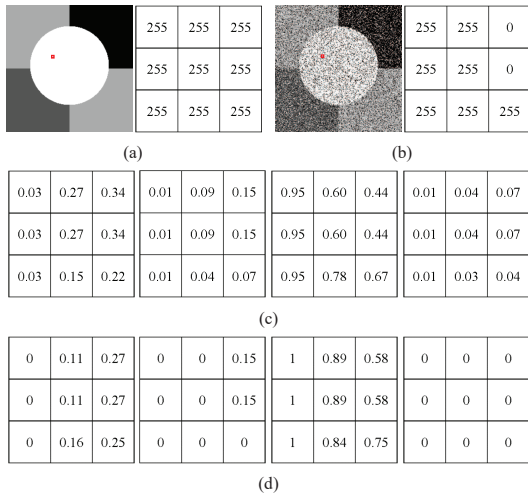


Fig. 4. Comparison of partition matrices produced by the FCM algorithm and sparse regularization-based FCM ($c = 4$, $\alpha = 2$, and $\beta = 0.01$). (a) Original synthetic image included four gray levels (0, 85, 170, 255). (b) Image corrupted by SPIN ($r = 35\%$). (c) Membership partition using FCM. (d) Membership partition using sparse regularization-based FCM.

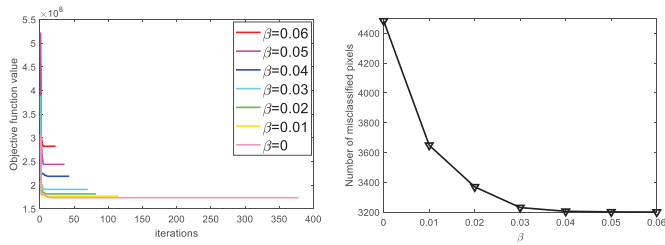


Fig. 5. The rates of convergence and classification errors on Fig. 4(b) with different values of β .

Fig. 5 exhibits the effect of the sparse ℓ_0 -norm regularization on the rate of convergence and classification errors. Since MGR can optimize the data distribution to further enhance the rate of convergence of FCM, we only impose the sparse ℓ_0 -norm regularization on FCM without considering image filtering, i.e., $\alpha = 0$. When $\beta = 0$, the sparse ℓ_0 -norm regularization has no impact on FCM, and the number of iterations comes up to maximum. As the values of β increase, the rate of convergence of FCM becomes higher and the number of misclassified pixels becomes smaller.

It is important to claim here that the value of β cannot be set too large. Although a larger β can make FCM converge faster, it could also increase the likelihood of producing incorrect membership partitions since prototypes are randomly initialized. Moreover, if β is greater than the maximum degree of membership where any image pixel is assigned to multiple clusters, FCM will not converge. Therefore, when setting β , it is necessary to experimentally increase its value from 0 and run the experiment several times in order to achieve the optimal segmentation.

D. Label Filtering via MGR

In order to further reduce the misclassification rate of clustering, we use MGR to filter labels of image pixels. For

$j = 1, 2, \dots, K$, target label ψ_j states that pixel f_j belongs to the i th cluster. It is defined as

$$\psi_j = \text{label}(\max\{u_{1j}, u_{2j}, \dots, u_{cj}\}),$$

where label denotes the location of maximum u_{ij} , i.e., $\psi_j = i$. Thus, we can define the label set of image pixels as

$$\Psi = \{\psi_j\} = \{\text{label}(\max\{u_{1j}, u_{2j}, \dots, u_{cj}\})\}, \quad (8)$$

for $j = 1, 2, \dots, K$. We reformulate label set Ψ in a matrix form with size $M \times N$. Thus a label image, denoted as Ψ_{im} , can be obtained. We use MGR to filter the original label image Ψ_{im} , then generating a filtered label image $\bar{\Psi}_{im}$ that is denoted as $\bar{\Psi}_{im} = \mathcal{R}^C(\Psi_{im})$. Here, we show an example to verify the advantage of label filtering.

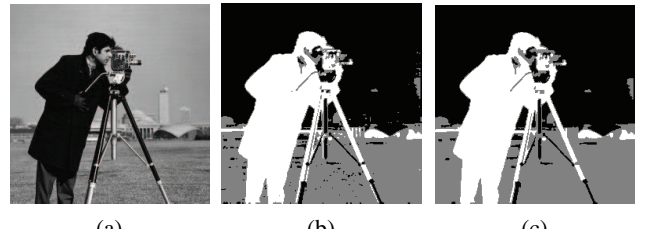


Fig. 6. Comparison between the original and filtered label images. From left to right: (a) ground image; (b) original label image; (c) filtered label image.

Fig. 6 gives the comparison between original and filtered label images. We can find the filtered label image is closer to the original image.

Based on the filtered label image $\bar{\Psi}_{im}$ and the obtained prototypes \mathbf{V} , the segmented feature set $\tilde{\mathbf{X}}$ is obtained. Then we can reconstruct a segmented image \tilde{f} using wavelet frame reconstruction \mathcal{W}^T :

$$\tilde{f} = \mathcal{W}^T(\tilde{\mathbf{X}}). \quad (9)$$

The proposed algorithm is realized in **Algorithm 1**.

Algorithm 1 Sparse regularization-based FCM algorithm incorporating MGR and tight wavelet frames (SRFCM)

Input: Image f , threshold ϵ , fuzziness coefficient m , and number of clusters c .

Output: Segmented image \tilde{f} .

- 1: Calculate filtered image \bar{f} based on (1)
 - 2: Calculate feature sets \mathbf{X} and $\tilde{\mathbf{X}}$ based on $\mathcal{W}f$ and $\mathcal{W}\bar{f}$
 - 3: Initialize randomly prototypes $\mathbf{v}_i^{(0)}$
 - 4: $t \leftarrow 1$
 - 5: **repeat**
 - 6: Use prototypes $\mathbf{v}_i^{(t-1)}$ to update partition matrix $\mathbf{U}^{(t)}$ based on (4), (5), (6)
 - 7: Use partition matrix $\mathbf{U}^{(t)}$ to update prototypes $\mathbf{v}_i^{(t)}$ based on (7)
 - 8: $t \leftarrow t + 1$
 - 9: **until** $\|\mathbf{U}^{(t)} - \mathbf{U}^{(t-1)}\| < \epsilon$
 - 10: **return** partition matrix \mathbf{U} and prototypes \mathbf{v}_i
 - 11: Generate labels of image pixels based on (8)
 - 12: Use MGR to filter labels
 - 13: Generate a segmented image \tilde{f} based on (9)
-

To assess the segmentation performance of different FCM-related algorithms, we adopt two objective performance indices, i.e., segmentation accuracy (SA) [43] and entropy-based information (EI) [44].

SA is often employed to evaluate segmentation effects on target images with known ground truth, which is formulated as

$$SA = (TP + TN) / (FN + FP + TP + TN),$$

where TP , FP , TN , and FN are the number of true positive, false positive, true negative, and false negative, respectively.

For target images without ground truth, EI is often used to assess the performance of segmentation algorithms, which is formulated as

$$EI = H_1(\tilde{f}) + H_2(\tilde{f}),$$

where $H_1(\tilde{f})$ is the expected region entropy of segmented image \tilde{f} , which is defined as

$$H_1(\tilde{f}) = \sum_{i=1}^c \frac{|A_i| H(A_i)}{|\tilde{f}|}$$

with the entropy for A_i is defined as

$$H(A_i) = - \sum_{z \in Z_i} \frac{|A_i(z)|}{|A_i|} \log \frac{|A_i(z)|}{|A_i|}.$$

Here, $A_i(z)$ denotes the set of pixels in A_i whose gray level values equal to z , and Z_i represents the set of all gray level values in A_i . Moreover, $H_2(\tilde{f})$ denotes the layout entropy of segmented image \tilde{f} , which is defined as

$$H_2(\tilde{f}) = - \sum_{i=1}^c \frac{|A_i| \log \frac{|A_i|}{|\tilde{f}|}}{|\tilde{f}|}$$

The aim of EI is to minimize the uniformity across the clusters while maximizing the uniformity of pixels within each segmented cluster. Hence, the smaller the EI value is, the better the segmentation effect is achieved.

V. EXPERIMENTAL STUDY

In the following, we mostly conduct ablation studies and report numerical results on a collection of synthetic, medical, and color images. Moreover, we also provide segmentation comparisons between SRFCM and other existing algorithms available in the literature, i.e., ‘FCM_S1’ [16], ‘FCM_S2’ [16], ‘EnFCM’ [24], ‘FGFCM’ [25], FLICM [26], ‘KWFLICM’ [17], ‘ARKFCM’ [28], ‘FDCM’ [18], ‘FRFCM’ [19], and ‘WFCM’ [14]. The comparisons are done both visually and quantitatively.

A. Parameter Setting

Prior to the numerical implementation of SRFCM and other algorithms, we require to set several parameters. All algorithms except FDCM consider spatial information of observed images. Therefore, for fair comparison, a local window with size 3×3 is set for these algorithms with the usage of spatial information. The fuzziness coefficient $m = 2$ and threshold $\epsilon = 10^{-6}$ are the same in all algorithms. The suitable number

of clusters c is assumed to be known, and preset the same for all algorithms.

Except for common parameters m , ϵ , and c , according to [16], [24], α in FCM_S1, FCM_S2, and EnFCM is exponentially set to 3.8, which aims to control the effect of the neighbors term. In FGFCM, the spatial scale factor and the gray-level scale factor are $\lambda_s = 3$ and $\lambda_g = 5$, respectively. FLICM, KWFLICM and ARKFCM are free of other parameters. Since FDCM conducts clustering based on super pixels, the number of super pixels is set to 800 according to the statement in [18]. Moreover, $\lambda = 0.5$ and $\alpha = 1.2$ are set for FDCM. For FRFCM, the mask image is the observed image, and a square structuring element of size 3×3 is used to obtain marker image. In addition, median filter is used to fuzzy membership filtering, and the filtering window is also 3×3 . As to WFCM, according to parameter settings in [14], μ aims to control the impact of the filtered term, thus is determined experimentally within the range $\mu \in [0.55, 0.65]$. Moreover, the 1-level wavelet frame transform is used.

We subsequently discuss the setting of the remaining parameters of the SRFCM. In image pixel filtering, we consider the observed image as the mask image, and use a square of size 3×3 as the structuring element to obtain the marker image. Similar to these settings, in the processing of label filtering, the original label image is taken as the mask image, and the structuring element of size 3×3 is adopted again. For the tight wavelet frame transform, we generally adopt 1-level wavelet frame transform to test all experiments, since the usage of higher levels only slightly improves segmentation results while computational costs are distinctly increased. This conclusion has been illustrated by the recent work in [14], [23], [45].

In addition, β is determined by the specific image. By testing a large number of images, we choose the value of $\beta \in [0, 0.06]$ experimentally. For selection of α in (2), we here take an example to show how to determine the value range of α . We take a set of its values to test its effect on the performance with the five images (see Fig. 8) contaminated by 35% SPIN. As shown in Fig. 7, through the numerical simulation, there are almost no apparent changes after generally setting $\alpha = 2$, which implies that the performance is rather stable. In fact, if α is too large, one will bring high computational cost and reset parameter β . However, if α is too small, the impact of noise on FCM will become highly visible. Therefore, we generally set $\alpha = 2$.

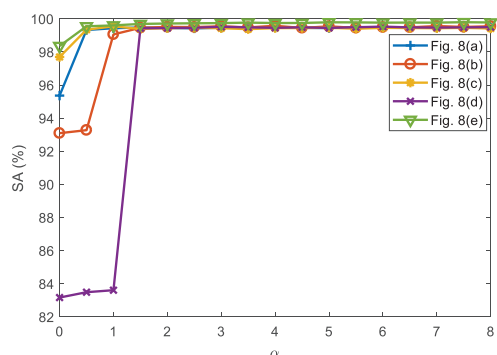


Fig. 7. Segmentation accuracy values with changes of α .

B. Ablation Studies and Analysis

As mentioned previously, there exist four key components play crucial roles in the proposed algorithm, i.e., image filtering, wavelet frames, sparse regularization, and label filtering. To better exhibit the effectiveness of each component of the proposed algorithm, we perform the ablation experiments and analyze their results. We impose 35% SPIN on the image shown in Fig. 8(a). The number of cluster is set to 4. Specific experimental details are summarized in TABLE II. In particular, in TABLE II, symbol \checkmark means that one component in the proposed algorithm is considered to enable while symbol \times represents the component is absent. The average SA values and iterations are obtained after the multiple runs of the proposed algorithm.

TABLE II
INVESTIGATION OF EACH COMPONENT OF THE PROPOSED ALGORITHM

Image filtering	Wavelet frames	Sparse regularization	Label filtering	SA (%)	Iterations
\times	\times	\times	\times	93.821	132
\checkmark	\times	\times	\times	97.615	89
\times	\checkmark	\times	\times	95.057	116
\times	\times	\checkmark	\times	94.372	37
\times	\times	\times	\checkmark	94.325	132
\checkmark	\checkmark	\checkmark	\times	99.584	15
\checkmark	\checkmark	\times	\checkmark	99.633	74
\checkmark	\times	\checkmark	\checkmark	98.486	16
\times	\checkmark	\checkmark	\checkmark	96.669	26
\checkmark	\checkmark	\checkmark	\checkmark	99.738	15

Obviously, we test 10 different combinations of the four key components. Without any innovation, the SA result of FCM is only 93.821%. When each component is considered separately, the SA results are improved by 3.794%, 1.236%, 0.551%, and 0.504%, respectively. The highest performance is obtained when all four components are available while the performance is lowest when any component is absent. We also observe that adding other three components in the absence of image filtering can only improve the SA results to a certain extent. In addition, the sparse regularization can significantly reduce iterations of clustering.

C. Results for Synthetic Images

In this subsection, we first test the performance of SRFCM and other algorithms for five synthetic images with size 256×256 (refer to Fig. 8). The numbers of clusters are 4, 4, 4, 3, and 3, respectively. These images are with ground truth and corrupted by AWGN and SPIN of high intensities.

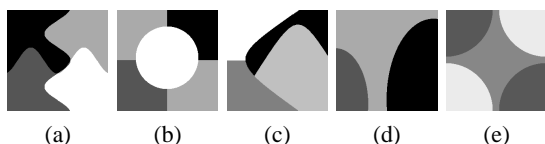


Fig. 8. Five synthetic images with ground truth.

Fig. 9 and 10 illustrate the visual comparison results for segmenting images (as shown in Fig. 8) contaminated by AWGN ($s = 30$) and SPIN ($r = 30\%$), respectively. It is clearly seen that FCM_S1, FCM_S2, EnFCM, FGFCM, FLICM and ARKFCM are not of robustness to AWGN of

high levels. Even though KWFLICM, FDCM, FRFCM and WFCM can remove AWGN sufficiently, they cannot preserve image edges and thus change image details to different extent. In addition, except for FDCM and FRFCM, other comparison algorithms cannot remove SPIN well. Although FDCM and FRFCM remove a large proportion of SPIN, image edges are obviously changed to some extent. In comparison with these algorithms, SRFCM truly maintains clear image edges and acquires better segmentation results. In the light of visual effects in Figs. 9 and 10, we can conclude that SRFCM is effective for removing AWGN and SPIN of high levels and preserving image details.

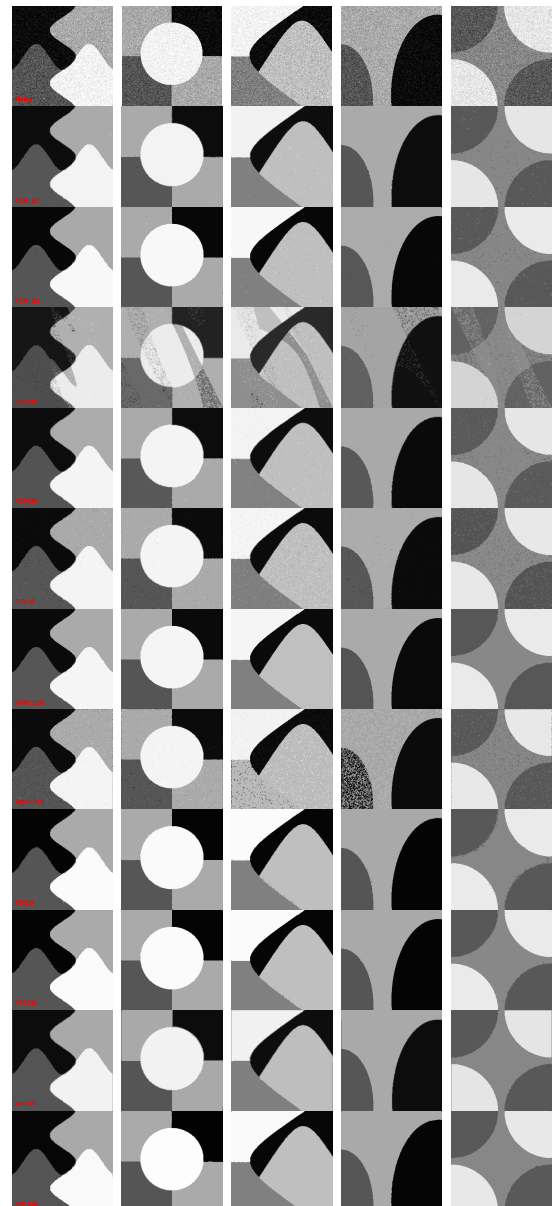


Fig. 9. Segmentation results with AWGN ($s = 30$). The parameters: $\beta_1 = 0.02$, $\beta_2 = 0.03$, $\beta_3 = 0.04$, $\beta_4 = 0.03$, and $\beta_5 = 0.05$. From top to bottom: noisy images and results of FCM_S1, FCM_S2, EnFCM, FGFCM, FLICM, KWFLICM, ARKFCM, FDCM, FRFCM, WFCM, and SRFCM.

TABLE III covers SA results corresponding to Figs. 9 and 10. The results of SRFCM are highlighted by the bold letter.

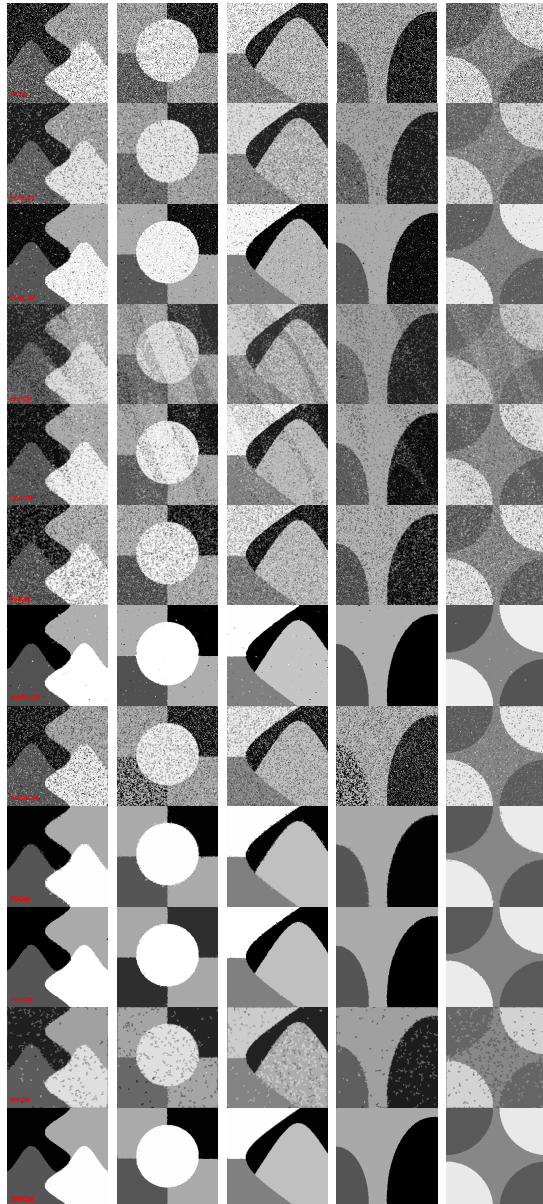


Fig. 10. Segmentation results with SPIN ($r = 30\%$). The parameters: $\beta_1 = 0.06$, $\beta_2 = 0.04$, $\beta_3 = 0.06$, $\beta_4 = 0.05$, and $\beta_5 = 0.04$. From top to bottom: noisy images and results of FCM_S1, FCM_S2, EnFCM, FGFCM, FLICM, KWFLICM, ARKFCM, FDCM, FRFCM, WFCM, and SRFCM.

We can clearly observe that SA values obtained by SRFCM are larger than those of other ten algorithms. Note that SA values of SRFCM are up to 99.997% for the case with AWGN on Fig. 8(c). In conclusion, other algorithms cannot work well in presence of noise of high levels, but SRFCM still reveals strong segmentation ability.

To further expose the performance of the proposed algorithm, we test five synthetic images without ground truth (refer to Fig. 11). In all data, we set the number of clusters set to 2. Figs. 12 and 13 show that segmentation effects of eleven algorithms. The segmentation results demonstrate that SRFCM is superior to other algorithms. SRFCM removes almost all noise and retains image contours. TABLE IV describes EI results for segmenting five synthetic images with AWGN and

TABLE III
SA RESULTS ON FIVE SYNTHETIC IMAGES WITH GROUND TRUTH

Method	Noise level	Fig. 8(a)	Fig. 8(b)	Fig. 8(c)	Fig. 8(d)	Fig. 8(e)
FCM_1	$s = 30$	99.711	99.780	99.699	99.712	99.963
	$r = 30\%$	92.725	91.978	96.635	77.496	91.777
FCM_2	$s = 30$	99.872	99.912	99.858	99.849	99.951
	$r = 30\%$	98.162	98.326	98.955	98.248	98.564
EnFCM	$s = 30$	99.200	95.346	99.397	82.886	99.432
	$r = 30\%$	92.156	85.507	77.271	76.041	86.919
FGFCM	$s = 30$	99.654	99.738	99.493	99.559	99.754
	$r = 30\%$	95.386	92.447	74.062	92.133	91.266
FLICM	$s = 30$	99.723	99.695	99.860	99.567	99.908
	$r = 30\%$	87.517	87.183	71.181	86.139	88.489
KWFLICM	$s = 30$	99.987	99.988	99.988	99.977	99.966
	$r = 30\%$	99.701	99.661	99.611	99.801	99.701
ARKFCM	$s = 30$	99.486	99.371	99.030	92.484	99.443
	$r = 30\%$	92.069	85.248	94.325	80.632	95.824
FDCM	$s = 30$	99.926	99.928	99.985	99.886	99.925
	$r = 30\%$	99.678	99.646	99.539	99.536	99.666
FRFCM	$s = 30$	99.985	99.983	99.991	99.948	99.957
	$r = 30\%$	99.802	99.796	99.757	99.742	99.826
WFCM	$s = 30$	99.614	99.123	99.565	99.600	99.223
	$r = 30\%$	98.819	96.353	99.380	97.906	97.363
SRFCM	$s = 30$	99.996	99.996	99.997	99.987	99.976
	$r = 30\%$	99.914	99.909	99.891	99.810	99.872

SPIN of high intensities. Compared with other algorithms, we can find that SRFCM can acquire smaller EI values. Similarly, it is concluded that SRFCM is of robustness to noise and keep more image details than other compared algorithms.

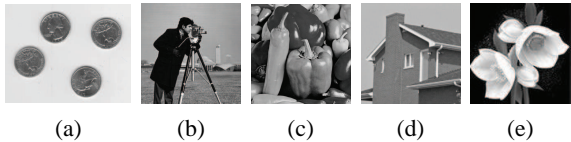


Fig. 11. Five synthetic images without ground truth.

D. Results for Medical Images

In this subsection, we test magnetic resonance images (MRIs) to illustrate the performance of eleven mentioned algorithms. These images are borrowed from a public brain database (BrainWeb): <http://www.bic.mni.mcgill.ca/brainweb/>. We here choose MRIs by T1 modality with slice thickness of 1mm resolution, 9% noise and 20% intensity non-uniformity. Five slices in the axial plane with the sequence of 70, 80, 90, 100, and 110, respectively, as shown in the first column of Fig. 14.

Fig. 14 shows the segmentation results for five MRIs. We set numbers of clusters to all 4. The quantitative comparison results are given in TABLE V. As shown in Fig. 14, SRFCM is more effective for noise removal and detail-preservation in MRIs than other FCM-related algorithms. TABLE V indicates that SA results of SRFCM are larger than those of other algorithms. Notice that SA values of SRFCM come up to 99.156% for the fourth slice in Fig. 14. On the account of experimental results in Fig. 14 and TABLE V, we conclude that SRFCM has a better segmentation ability for MRIs than other existing algorithms.

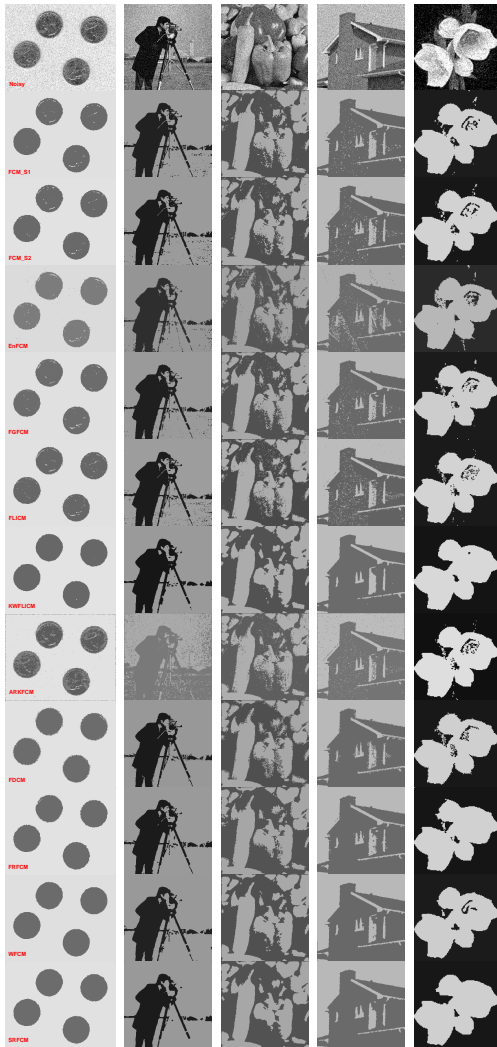


Fig. 12. Segmentation results with AWGN ($s = 30$ and $\beta = 0.04$). From top to bottom: noisy images and results of FCM_S1, FCM_S2, EnFCM, FGFCM, FLICM, KWFLICM, ARKFCM, FDCM, FRFCM, WFCM, and SRFCM.

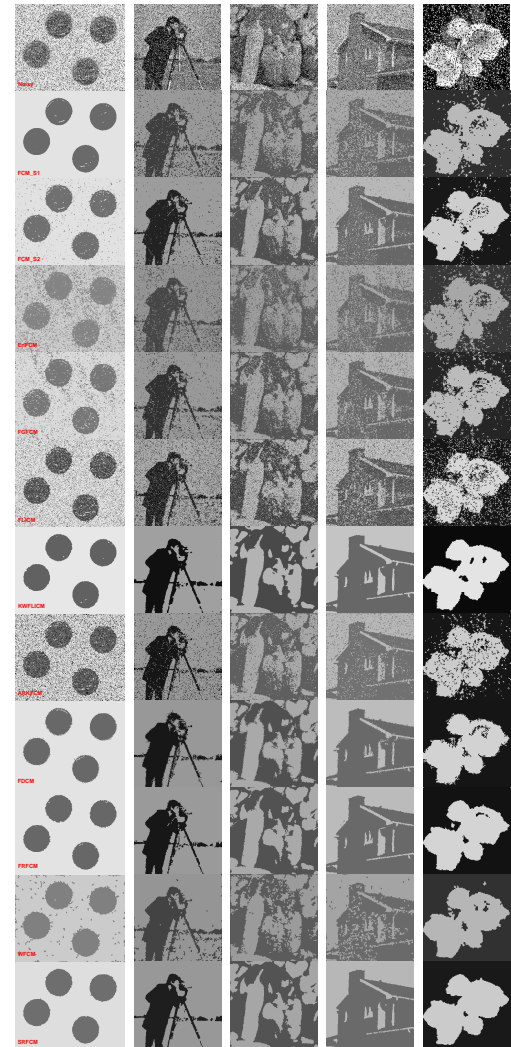


Fig. 13. Segmentation results with SPIN ($r = 30\%$ and $\beta = 0.05$). From top to bottom: noisy images and results of FCM_S1, FCM_S2, EnFCM, FGFCM, FLICM, KWFLICM, ARKFCM, FDCM, FRFCM, WFCM, and SRFCM.

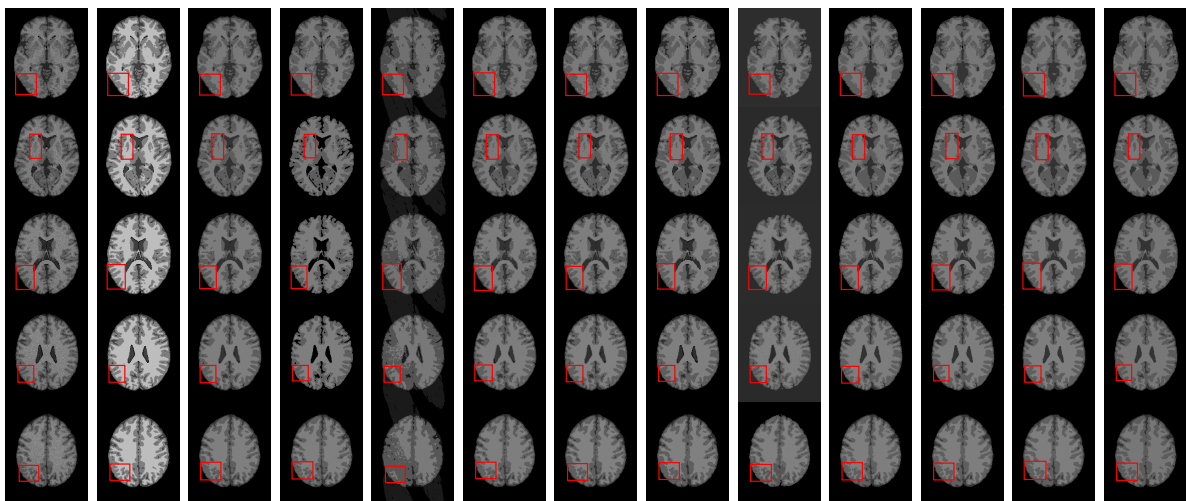


Fig. 14. Segmentation results on different MRIs ($\beta = 0.04$). From left to right: noisy images, ground truth, and results of FCM_S1, FCM_S2, EnFCM, FGFCM, FLICM, KWFLICM, ARKFCM, FDCM, FRFCM, WFCM, and SRFCM.

TABLE IV
EI RESULTS ON FIVE SYNTHETIC IMAGES WITHOUT GROUND TRUTH

Method	Noise level	Fig. 11(a)	Fig. 11(b)	Fig. 11(c)	Fig. 11(d)	Fig. 11(e)
FCM_1	$s = 30$	1.482	2.139	2.307	1.991	1.963
	$r = 30\%$	1.633	2.248	2.433	2.146	2.017
FCM_2	$s = 30$	1.483	2.139	2.307	1.996	1.963
	$r = 30\%$	1.528	2.184	2.377	2.063	1.995
EnFCM	$s = 30$	1.489	2.159	2.350	2.031	1.981
	$r = 30\%$	1.673	2.276	2.461	2.172	2.050
FGFCM	$s = 30$	1.486	2.150	2.320	2.002	1.970
	$r = 30\%$	1.604	2.236	2.423	2.125	2.037
FLICM	$s = 30$	1.481	2.140	2.323	2.014	1.965
	$r = 30\%$	1.658	2.290	2.468	2.173	2.093
KWFLICM	$s = 30$	1.483	2.139	2.294	1.975	1.966
	$r = 30\%$	1.486	2.151	2.295	1.975	1.978
ARKFCM	$s = 30$	1.485	2.229	2.324	2.015	1.961
	$r = 30\%$	1.690	2.227	2.383	2.072	2.046
FDCM	$s = 30$	1.486	2.136	2.324	1.992	1.965
	$r = 30\%$	1.485	2.153	2.313	1.989	1.984
FRFCM	$s = 30$	1.484	2.136	2.304	1.980	1.966
	$r = 30\%$	1.485	2.145	2.296	1.978	1.973
WFCM	$s = 30$	1.483	2.141	2.303	1.978	1.966
	$r = 30\%$	1.538	2.204	2.378	2.078	1.983
SRFCM	$s = 30$	1.480	2.128	2.290	1.975	1.964
	$r = 30\%$	1.484	2.144	2.287	1.965	1.966

TABLE V
SA RESULTS ON FIVE MRIs

Method	Fig. 14 row 1	Fig. 14 row 2	Fig. 14 row 3	Fig. 14 row 4	Fig. 14 row 5
FCM_1	98.126	98.355	98.699	98.882	95.473
FCM_2	98.350	98.409	98.702	98.890	98.691
EnFCM	96.448	95.346	95.919	97.283	97.866
FGFCM	97.625	97.479	97.976	98.210	95.644
FLICM	98.304	98.355	98.747	98.887	98.722
KWFLICM	97.334	97.917	98.042	98.541	98.536
ARKFCM	98.747	98.330	98.801	98.915	96.397
FDCM	97.782	97.943	98.531	98.561	98.434
FRFCM	97.912	97.971	98.536	98.651	98.574
WFCM	97.497	97.604	98.203	98.399	98.529
SRFCM	98.863	98.457	98.931	99.156	98.941

E. Results for Color Images

To further illustrate good performance of SRFCM, we test a collection of Red-Green-Blue (RGB) color images. Generally speaking, most of improved FCM-related algorithms are weak for segmenting color images due to difficult acquisition of spatial information of color images. However, SRFCM overcomes this drawback. It is easy to extend multivariate MGR to color images [46]. For the wavelet frame transform, we respectively apply it in each channel of RGB color images. Thus, the dimensionality of feature spaces of a color image is three times higher than that of a gray image. The other steps of color image segmentation are similar to those applied to gray image segmentation. We segment two sets of color images to illustrate multiphase segmentation effects of the proposed algorithm.

In the first experiments, we select six color images obtained from the Berkeley Segmentation Dataset (BSDS300): <https://www2.eecs.berkeley.edu/Research/Projects/CS/vision/bsds/BSDS300/html/dataset/images.html>. We conduct related experiments and the corresponding results are shown in Fig. 15 and TABLE VI. We set numbers of clusters of six images to 2, 2, 2, 3, 2, and 2. As shown in Fig. 15,

other compared algorithms are deficient for retaining true image contours. In contrast, SRFCM clearly describes accurate image details and makes clustering results close to object segmentation results. TABLE VI shows the corresponding EI values of all algorithms for segmenting six color images. SRFCM's EI results are generally lower than those produced by other algorithms. Therefore, it is concluded that SRFCM can achieve excellent segmentation performance for color images.

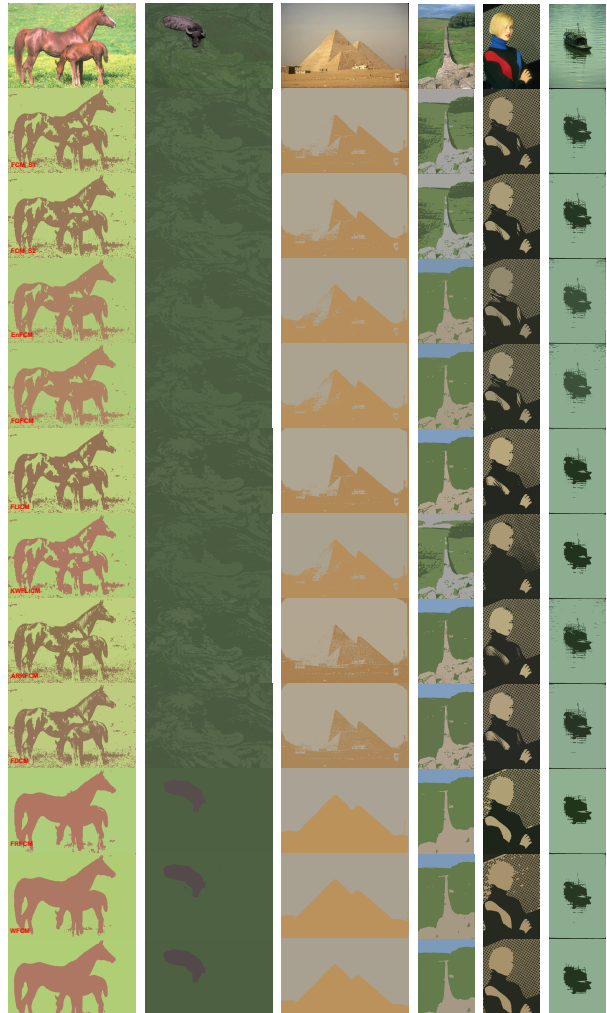


Fig. 15. Segmentation results on six color images in BSDS300. The parameters: $\beta_1 = 0.04$, $\beta_2 = 0.03$, $\beta_3 = 0.04$, $\beta_4 = 0.05$, $\beta_5 = 0.06$, and $\beta_6 = 0.05$. From top to bottom: original image and results of FCM_S1, FCM_S2, EnFCM, FGFCM, FLICM, KWFLICM, ARKFCM, FDCM, FRFCM, and WFCM.

Besides color images in BSDS300, we also consider real images, i.e., Global Earth observation data obtained from the NASA Earth Observation data set: <http://neo.sci.gsfc.nasa.gov/>. There exists unknown noise in sampled images due to bit errors appearing in satellite measurements. We segment two real images showing sea ice and snow extent and chlorophyll concentration as typically shown in Figs. 16 and 17. Each image corresponds to a specific scene. Each scene is randomly shot 50 times from 2000 to 2019. The mean image of the 50 shots is roughly taken as the ‘reference (original) image’, with

TABLE VI
EI RESULTS ON SIX COLOR IMAGES IN BSDS300

Method	Fig. 15 column 1	Fig. 15 column 2	Fig. 15 column 3	Fig. 15 column 4	Fig. 15 column 5	Fig. 15 column 6
FCM_1	2.247	1.670	1.999	2.173	2.199	2.076
FCM_2	2.281	1.665	1.995	2.170	2.200	2.077
EnFCM	2.284	1.730	2.047	2.270	2.250	2.094
FGFCM	2.269	1.701	2.023	2.191	2.231	2.083
FLICM	2.234	1.656	2.113	2.266	2.201	2.073
KWFLICM	2.260	1.618	2.140	2.319	2.216	2.083
ARKFCM	2.239	1.639	1.921	2.173	2.198	2.071
FDCM	2.199	1.614	2.081	2.159	2.192	2.069
FRFCM	2.150	1.517	2.038	2.218	2.143	1.982
WFCM	2.148	1.518	2.040	2.219	2.116	1.983
SRFCM	2.035	1.462	1.814	2.032	2.019	1.963

which the EI can be computed. EI results are summarized in TABLE VII.

TABLE VII
EI RESULTS ON TWO REAL IMAGES IN NASA

Method	First image	Second image
FCM_1	0.871	1.500
FCM_2	0.852	1.502
EnFCM	1.027	1.516
FGFCM	0.884	1.511
FLICM	0.859	1.488
KWFLICM	0.831	1.499
ARKFCM	0.829	1.485
FDCM	0.833	1.504
FRFCM	0.815	1.370
WFCM	0.817	1.395
SRFCM	0.766	1.304

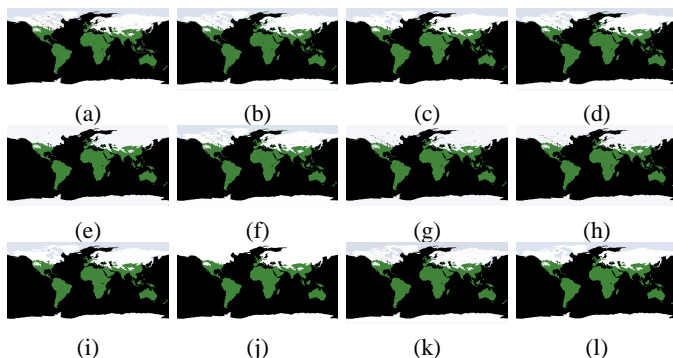


Fig. 16. Segmentation results on sea ice and snow extent ($\beta = 0.03$). From (a) to (l): noisy image and results of FCM_S1, FCM_S2, EnFCM, FGFCM, FLICM, KWFLICM, ARKFCM, FDCM, FRFCM, WFCM, and SRFCM.

Fig. 16 illustrates the results for segmenting sea ice and snow extent. The colors on images shown in Fig. 16 represent where the land and ocean are covered by snow and ice per week (here is February 7–14, 2015). We set the number of clusters to 4. Fig. 17 shows the segmentation results on chlorophyll concentration. The colors represent where and how much phytoplankton are growing over a span of days. The black areas show where the satellite could not measure phytoplankton. The number of clusters is set to 2. As shown in Figs. 16 and 17, the segmentation results of most of algorithms including FCM_S1, FCM_S2, EnFCM, FGFCM, FLICM, KWFLICM, ARKFCM and FDCM show that they can retain clear edges but cannot sufficiently remove unknown noise. Differing from them, FRFCM and WFCM perform well for noise removal. However, the two algorithms bring over-

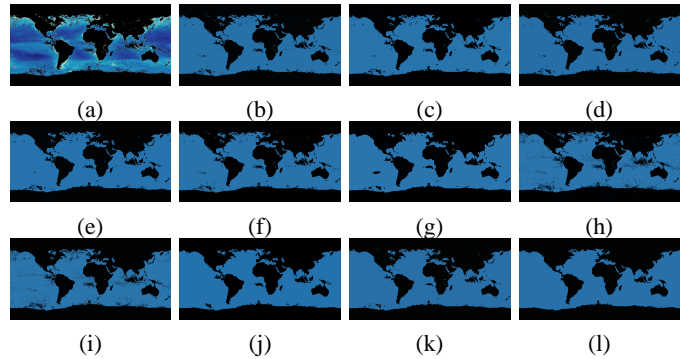


Fig. 17. Segmentation results on chlorophyll concentration ($\beta = 0.04$). From (a) to (l): noisy image and results of FCM_S1, FCM_S2, EnFCM, FGFCM, FLICM, KWFLICM, ARKFCM, FDCM, FRFCM, WFCM, and SRFCM.

smoothing to some extent, thus resulting in several topology changes, such as merging and splitting. Superior to other algorithms, SRFCM can not only extensively suppress unknown noise, but also retain clear contours in images. According to these practical examples, we can conclude that the above ten algorithms do not have good performance for preserving object features and removing noise simultaneously. SRFCM makes up this drawback successfully and works better than them.

F. Running Time

To compare the practical facets of above algorithms, we show comparisons of computational costs of above experiments. All experiments are realized in MATLAB on a laptop with Intel(R) Xeon(R) W-2133 CPU of (3.60 GHz) and 32.0 GB RAM. The average computational costs of all algorithms on tested images, including synthetic images with ground truth, synthetic images without ground truth, medical images, color images and real images, are given in TABLE VIII. In addition, we also visually exhibit the difference between average computational costs of all algorithms in Fig. 18.

TABLE VIII
AVERAGE COMPUTATION COSTS (IN SECONDS) ON DIFFERENT IMAGES

Method	Synthetic images with ground truth	Synthetic images without ground truth	Medical images	Color images	Real images
FCM_1	20.00	17.50	14.50	56.59	63.10
FCM_2	21.33	16.02	16.54	58.03	61.56
EnFCM	1.00	1.01	1.23	1.82	2.36
FGFCM	1.28	1.27	1.36	2.88	3.30
FLICM	4.15	3.91	4.23	5.27	5.86
KWFLICM	24.04	39.14	35.35	115.54	176.19
ARKFCM	6.05	4.81	4.47	8.60	18.42
FDCM	12.07	16.61	22.96	69.38	72.36
FRFCM	0.24	0.23	0.22	1.23	3.21
WFCM	3.08	3.04	3.47	6.17	6.35
SRFCM	2.75	2.47	3.05	5.80	5.52

As shown in TABLE VIII and Fig. 18, it is obvious that KWFLICM is the most time-consuming for gray image segmentation. Moreover, FCM_S1, FCM_S2 and FDCM also exhibits high computational complexity. FRFCM is the most time-saving for all experiments due to the usage of gray level histograms. EnFCM and FGFCM are very efficient. Although the three algorithms are faster than the proposed algorithm, their segmentation performance are worse than that

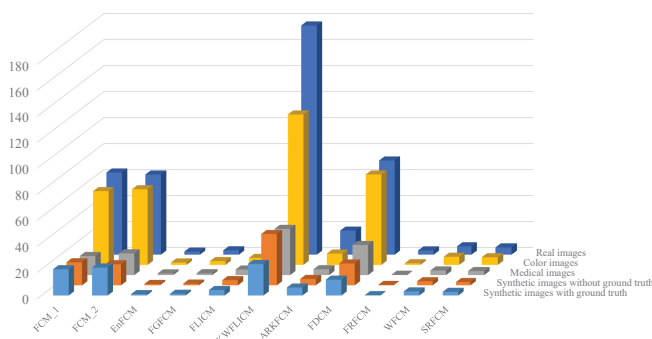


Fig. 18. Average computation costs (in seconds) on different images.

of SRFCM. When all mentioned algorithms are extended to color image segmentation, they require much more computational time due to the increase of dimensionality of image data. Especially, computational costs of FCM_S1, FCM_S2, KWFLCM and FDCM are extremely large. EnFCM, FGFCM, PRFCM and SRFCM are significantly faster than other algorithms. Compared with EnFCM, FGFCM and PRFCM, SRFCM spends a little more time. On account of its better segmentation effect, this drawback can be tolerated. Moreover, since SRFCM has acceptable computation costs and better performance simultaneously, it can be applied to a wide range of practical fields.

VI. CONCLUSIONS

The existing FCM-related algorithms mostly depend on the usage of spatial information and kernel distances to enhance the robustness of the conventional FCM algorithm. These algorithms usually exhibit high computational complexity even though they can realize clustering well. To deal with this issue, we report a sparse regularization-based FCM algorithm for image segmentation by incorporating MGR and a tight wavelet frame transform. To make FCM robust, we first utilize MGR to filter observed images. A wavelet frame system is employed to form feature spaces of observed and filtered images. Taking such feature sets as data to be clustered, we present an improved FCM algorithm in which a sparse regularization term is introduced into its objective function. To further enhance the segmentation accuracy, we use MGR to filter the label set generated by clustering. The segmentation effect of the proposed algorithm is illustrated through a collection of experiments. Finally, the crucial conclusions are drawn:

- 1) MGR improves simultaneously the noise-immunity and retention capacity of image details, which is a key step before further clustering. This means that MGR introduces spatial information of images into the objective function of FCM. MGR overcomes the shortcoming that different filters have to be chosen for different types of noise. Therefore, it makes FCM more robust to different types of noise. Moreover, its usage also makes distribution characteristics of image pixels adaptive to fuzzy clustering, thus enhancing the rate of convergence of clustering. In addition, MGR is also used to filter labels in the last step

of the proposed algorithm, then reduces the possibility of misclassification.

- 2) A wavelet frame system is employed to form feature sets of images, which removes the difficulty of the direct use of image pixels and makes information in images sufficiently analyzed and manipulated. In addition, the proposed algorithm can naturally be regarded as a kernel-based FCM algorithm when taking tight wavelet frames as a kernel function.
- 3) A sparse regularization term is introduced into the objective function of FCM, which gives rise to the strong sparsity of the partition matrix generated by FCM. Thus, it lowers the computational cost of the proposed algorithm. Moreover, the segmentation effect is slightly improved.
- 4) The proposed algorithm requires low computational cost. Although it has slightly lower computational efficiency than few FCM-related algorithms, its good performance can offset this drawback.
- 5) Numerical results show that the proposed algorithm is more capable of segmentation than other FCM-related algorithms. Hence, the proposed algorithm is more potential in applications.

Numerical results demonstrate sufficiently the effectiveness and practicability of the proposed algorithm. Nevertheless, there exist still some open issues worth exploring. For instance, in a future study, its application areas could be expanded to image segmentation in non-Euclidean spaces such as computer networks, 3D medical imaging and remote sensing [47], social networks, ecological systems [48], and transportation networks [49]. The automatic selection of numbers of clusters is also one of topics worth pursuing. In addition, it is also worth discussing how to choose mask and marker images in order to achieve better segmentation results.

APPENDIX

We consider the minimization of the energy function

$$E = \sum_{i=1}^c \sum_{j=1}^K \eta_{ij}^m (\|\mathbf{x}_j - \mathbf{v}_i\|^2 + \alpha \|\bar{\mathbf{x}}_j - \mathbf{v}_i\|^2),$$

subject to

$$\sum_{i=1}^c \eta_{ij} = 1, \text{ for } j = 1, 2, \dots, K.$$

We apply the Lagrangian multiplier method to solve the minimization problem. The Lagrangian function is defined as

$$\mathcal{L}_\Lambda(\boldsymbol{\eta}, \mathbf{V}) := \sum_{i=1}^c \sum_{j=1}^K \eta_{ij}^m d_{ij} + \sum_{j=1}^K \lambda_j \cdot \left(\sum_{i=1}^c \eta_{ij} - 1 \right), \quad (10)$$

where $\Lambda = \{\lambda_j\}_{j=1,2,\dots,K}$ is a set of Lagrangian multipliers, and $d_{ij} = \|\mathbf{x}_j - \mathbf{v}_i\|^2 + \alpha \|\bar{\mathbf{x}}_j - \mathbf{v}_i\|^2$.

First, by fixing \mathbf{V} , we minimize (10) with respect to $\boldsymbol{\eta}$. Thus, we have

$$\frac{\partial \mathcal{L}_\Lambda}{\partial \eta_{ij}} = m d_{ij} \eta_{ij}^{m-1} + \lambda_j = 0.$$

We obtain

$$\eta_{ij} = \left(\frac{-\lambda_j}{m} \right)^{\frac{1}{m-1}} \cdot (d_{ij})^{-\frac{1}{m-1}}. \quad (11)$$

Based on the constraint $\sum_{q=1}^c \eta_{qj} = 1$, we get

$$\begin{aligned} 1 &= \sum_{q=1}^c \eta_{qj} = \sum_{q=1}^c \left(\left(\frac{-\lambda_j}{m} \right)^{\frac{1}{m-1}} \cdot (d_{qj})^{-\frac{1}{m-1}} \right) \\ &= \left(\frac{-\lambda_j}{m} \right)^{\frac{1}{m-1}} \cdot \sum_{q=1}^c (d_{qj})^{-\frac{1}{m-1}}. \end{aligned}$$

Thus, we have

$$\left(\frac{-\lambda_j}{m} \right)^{\frac{1}{m-1}} = \frac{1}{\sum_{q=1}^c (d_{qj})^{-\frac{1}{m-1}}}. \quad (12)$$

Substitute (12) into (11), we get

$$\eta_{ij} = \frac{(d_{ij})^{-\frac{1}{m-1}}}{\sum_{q=1}^c (d_{qj})^{-\frac{1}{m-1}}}.$$

Next, by fixing $\boldsymbol{\eta}$, we minimize (10) in terms of \mathbf{V} . Thus, we have

$$\frac{\partial \mathcal{L}_\Lambda}{\partial \mathbf{v}_i} = \sum_{j=1}^K (-2) \cdot \eta_{ij}^m \cdot ((\mathbf{x}_j + \alpha \bar{\mathbf{x}}_j) - (\mathbf{v}_i + \alpha \mathbf{v}_i)) = 0.$$

Thus, we have

$$\sum_{j=1}^K \eta_{ij}^m (\mathbf{x}_j + \alpha \bar{\mathbf{x}}_j) = \sum_{j=1}^K \eta_{ij}^m (\mathbf{v}_i + \alpha \mathbf{v}_i).$$

The optimal \mathbf{v}_i is presented as

$$\mathbf{v}_i = \frac{\sum_{j=1}^K \eta_{ij}^m (\mathbf{x}_j + \alpha \bar{\mathbf{x}}_j)}{(1 + \alpha) \sum_{j=1}^K \eta_{ij}^m}.$$

REFERENCES

- [1] J. C. Dunn, "A fuzzy relative of the ISODATA process and its use in detecting compact well-separated clusters," *J. Cybernet.*, vol. 3, no. 3, pp. 32–57, 1973.
- [2] J. C. Bezdek, *Pattern Recognition with Fuzzy Objective Function Algorithms*. New York: Plenum Press, 1981.
- [3] J. de Jesús Rubio, "SOFMLS: online self-organizing fuzzy modified least-squares network," *IEEE Trans. Fuzzy Syst.*, vol. 17, no. 6, pp. 1296–1309, Dec. 2009.
- [4] J. de Jesús Rubio, D. Ricardo Cruz, I. Elias, G. Ochoa, R. Balcazarand, and A. Aguilar, "ANFIS system for classification of brain signals," *J. Intell. Fuzzy Syst.*, vol. 37, no. 3, pp. 4033–4041, Oct. 2019.
- [5] V. Grau, A. Mewes, M. Alcaniz, R. Kikinis, and S. Warfield, "Improved watershed transform for medical image segmentation using prior information," *IEEE Trans. Med. Imag.*, vol. 23, no. 4, pp. 447–458, Apr. 2004.
- [6] D. Mahapatra, "Semi-supervised learning and graph cuts for consensus based medical image segmentation," *Pattern Recognit.*, vol. 63, pp. 700–709, Mar. 2017.
- [7] C. N. Giap, L. H. Son, and F. Chiclana, "Dynamic structural neural network," *J. Intell. Fuzzy Syst.*, vol. 34, no. 4, pp. 2479–2490, Apr. 2018.
- [8] D. Pathak, P. Krähenbühl, and T. Darrell, "Constrained convolutional neural networks for weakly supervised segmentation," in *Proc. IEEE Int. Conf. Comput. Vis. (ICCV)*, Santiago, Dec. 2015, pp. 1796–1804.
- [9] J. de Jesús Rubio, E. Lughofer, J. A. Meda-Campaña, L. A. Páramo, J. F. Novoa, and J. Pacheco, "Neural network updating via argument Kalman filter for modeling of Takagi-Sugeno fuzzy models," *J. Intell. Fuzzy Syst.*, vol. 35, no. 2, pp. 2585–2596, Aug. 2018.
- [10] M. Gong, H. Li, X. Zhang, Q. Zhao, and B. Wang, "Nonparametric statistical active contour based on inclusion degree of fuzzy sets," *IEEE Trans. Fuzzy Syst.*, vol. 24, no. 5, pp. 1176–1192, Oct. 2016.
- [11] T. Lei, P. Liu, X. Jia, X. Zhang, H. Meng, and A. K. Nandi, "Automatic fuzzy clustering framework for image segmentation," *IEEE Trans. Fuzzy Syst.*, to be published, doi: 10.1109/TFUZZ.2019.2930030.
- [12] F. Zhao, J. Fan, H. Liu, R. Lan, and C. W. Chen, "Noise robust multiobjective evolutionary clustering image segmentation motivated by the intuitionistic fuzzy information," *IEEE Trans. Fuzzy Syst.*, vol. 27, no. 2, pp. 387–401, Feb. 2019.
- [13] F. Zhao, H. Liu, J. Fan, C. W. Chen, R. Lan, and N. Li, "Intuitionistic fuzzy set approach to multi-objective evolutionary clustering with multiple spatial information for image segmentation," *Neurocomputing*, vol. 312, pp. 296–309, Oct. 2018.
- [14] C. Wang, W. Pedrycz, J. Yang, M. Zhou, and Z. Li, "Wavelet frame-based fuzzy C-means clustering for segmenting images on graphs," *IEEE Trans. Cybern.*, to be published, doi: 10.1109/TCYB.2019.2921779.
- [15] M. Ahmed, S. Yamany, N. Mohamed, A. Farag, and T. Moriarty, "A modified fuzzy C-means algorithm for bias field estimation and segmentation of MRI data," *IEEE Trans. Med. Imag.*, vol. 21, no. 3, pp. 193–199, Aug. 2002.
- [16] S. Chen and D. Zhang, "Robust image segmentation using FCM with spatial constraints based on new kernel-induced distance measure," *IEEE Trans. Syst. Man Cybern. Part B Cybern.*, vol. 34, no. 4, pp. 1907–1916, Aug. 2004.
- [17] M. Gong, Y. Liang, J. Shi, W. Ma, and J. Ma, "Fuzzy C-means clustering with local information and kernel metric for image segmentation," *IEEE Trans. Image Process.*, vol. 22, no. 2, pp. 573–584, Feb. 2013.
- [18] J. Gu, L. Jiao, S. Yang, and F. Liu, "Fuzzy double c-means clustering based on sparse self-representation," *IEEE Trans. Fuzzy Syst.*, vol. 26, no. 2, pp. 612–626, Apr. 2018.
- [19] T. Lei, X. Jia, Y. Zhang, L. He, H. Meng, and K. N. Asoke, "Significantly fast and robust fuzzy c-means clustering algorithm based on morphological reconstruction and membership filtering," *IEEE Trans. Fuzzy Syst.*, vol. 26, no. 5, pp. 3027–3041, Oct. 2018.
- [20] L. Najman and M. Schmitt, "Geodesic saliency of watershed contours and hierarchical segmentation," *IEEE Trans. Pattern Anal. Mach. Intell.*, vol. 18, no. 12, pp. 1163–1173, Dec. 1996.
- [21] L. Vincent, "Morphological grayscale reconstruction in image analysis: applications and efficient algorithms," *IEEE Trans. Image Process.*, vol. 2, no. 2, pp. 176–201, Apr. 1993.
- [22] B. Dong and Z. Shen, "MRA-based wavelet frames and applications," in *The Mathematics of Image Processing* (IAS Lecture Notes Series). Salt Lake City, UT, USA: Park City Mathematics Institute, 2010.
- [23] J. F. Cai, B. Dong, S. Osher, and Z. Shen, "Image restoration: total variation, wavelet frames, and beyond," *J. Amer. Math. Soc.*, vol. 25, no. 4, pp. 1033–1089, May 2012.
- [24] L. Szilagyi, Z. Benyo, S. Szilagyi, and H. Adam, "MR brain image segmentation using an enhanced fuzzy C-means algorithm," in *Proc. 25th Annu. Int. Conf. IEEE EMBS*, Sep. 2003, pp. 724–726.
- [25] W. Cai, S. Chen, and D. Zhang, "Fast and robust fuzzy c-means clustering algorithms incorporating local information for image segmentation," *Pattern Recognit.*, vol. 40, no. 3, pp. 825–838, Mar. 2007.
- [26] S. Krinidis and V. Chatzis, "A robust fuzzy local information C-means clustering algorithm," *IEEE Trans. Image Process.*, vol. 19, no. 5, pp. 1328–1337, Jan. 2010.
- [27] Z. Zhao, L. Cheng, and G. Cheng, "Neighbourhood weighted fuzzy c-means clustering algorithm for image segmentation," *IET Image Process.*, vol. 8, no. 3, pp. 150–161, Mar. 2014.
- [28] A. Elazab, C. Wang, F. Jia, J. Wu, G. Li, and Q. Hu, "Segmentation of brain tissues from magnetic resonance images using adaptively regularized kernel-based fuzzy-means clustering," *Comput. Math. Method. M.*, vol. 2015, pp. 1–12, Nov. 2015.
- [29] X. Zhu, W. Pedrycz, and Z. W. Li, "Fuzzy clustering with nonlinearly transformed data," *Appl. Soft Comput.*, vol. 61, pp. 364–376, Dec. 2017.
- [30] R. R. Ghareeb, G. Gendy, A. Abdelfattah, and H. Selim, "Adaptive local data and membership based KL divergence incorporating C-means algorithm for fuzzy image segmentation," *Appl. Soft Comput.*, vol. 59, pp. 143–152, Oct. 2017.
- [31] K. P. Lin, "A novel evolutionary kernel intuitionistic fuzzy C-means clustering algorithm," *IEEE Trans. Fuzzy Syst.*, vol. 22, no. 5, pp. 1074–1087, Aug. 2014.

- [32] J. C. Bezdek, R. Ehrlich, and W. Full, "FCM: The fuzzy C-means clustering algorithm," *Comput. Geosci.*, vol. 10, no. 2-3, pp. 191–203, 1984.
- [33] J. Yang and C. Wang, "A developed Fuzzy C-Means algorithm for mesh segmentation," in *Proc. 11th Int. Cong. Image Signal Process., BioMed. Eng. Inf. (CISP-BMEI)*, Oct. 2018, pp. 1–5. doi: 10.1109/CISP-BMEI.2018.8633099.
- [34] J. Yang, E. Zhang, and C. Wang, "Color image segmentation via wavelet frames," in *Proc. IEEE 4th Int. Conf. Signal Image Process. (ICSIP)*, Jul. 2019, pp. 975–979.
- [35] D. Ma and C. Wang, "Removal of mixed Gaussian and impulse noise using data-driven tight frames," *J. Eng. Sci. Technol. Rev.*, vol. 11, no. 2, pp. 26–31, Mar. 2018.
- [36] C. Wang, Z. Yan, W. Pedrycz, M. Zhou, and Z. Li, "A weighted fidelity and regularization-based method for mixed or unknown noise removal from images on graphs," *IEEE Trans. Image Process.*, vol. 29, no. 1, pp. 5229–5243, Dec. 2020.
- [37] C. Wang and J. Yang, "Poisson noise removal of images on graphs using tight wavelet frames," *Visual Comput.*, vol. 34, no. 10, pp. 1357–1369, Oct. 2018.
- [38] B. Dong, Q. T. Jiang, C. Q. Liu, and Z. Shen, "Multiscale representation of surfaces by tight wavelet frames with applications to denoising," *Appl. Comput. Harmon. Anal.*, vol. 41, no. 2, pp. 561–589, Sep. 2016.
- [39] J. Yang and C. Wang, "A wavelet frame approach for removal of mixed Gaussian and impulse noise on surfaces," *Inverse Probl. Imaging*, vol. 11, no. 5, pp. 783–798, Oct. 2017.
- [40] A. Ron and Z. Shen, "Affine systems in $L_2(\mathbb{R}^d)$: The analysis of the analysis operator," *J. Funct. Anal.*, vol. 148, no. 2, pp. 408–447, Aug. 1997.
- [41] J. Chen, C. Su, W. Grimson, J. Liu, and D. Shiue, "Object segmentation of database images by dual multiscale morphological reconstructions and retrieval applications," *IEEE Trans. Image Process.*, vol. 21, no. 2, pp. 828–843, Feb. 2012.
- [42] J. Yang, G. Zhu, D. Tong, L. Lu, and Z. Shen, "B-spline tight frame based force matching method," *J. Comput. Phys.*, vol. 362, no. 1, pp. 208–219, Jun. 2018.
- [43] C. Li, R. Huang, Z. Ding, J. C. Gatenby, D. N. Metaxas, and J. C. Gore, "A level set method for image segmentation in the presence of intensity inhomogeneities with application to MRI," *IEEE Trans. Image Process.*, vol. 20, no. 7, pp. 2007–2016, Jul. 2011.
- [44] H. Zhang, J. Fritts, and S. Goldman, "An entropy-based objective evaluation method for image segmentation," in *Proc. SPIE, Storage Retrieval Methods Appl. Multimedia*, vol. 5307, Jan. 2004, pp. 38–49.
- [45] B. Dong, "Sparse representation on graphs by tight wavelet frames and applications," *Appl. Comput. Harmon. Anal.*, vol. 42, no. 3, pp. 452–479, May 2017.
- [46] T. Lei, Y. Zhang, Y. Wang, S. Liu, and Z. Guo, "A conditionally invariant mathematical morphological framework for color images," *Inf. Sci.*, vol. 387, pp. 34–52, May 2017.
- [47] T. Xu, L. Jiao, and W. J. Emery, "SAR image content retrieval based on fuzzy similarity and relevance feedback," *IEEE J. Sel. Topics Appl. Earth Observ. Remote Sens.*, vol. 10, no. 5, pp. 1824–1842, May 2017.
- [48] C. Wang, J. Chen, Z. Li, E. Nasr, and A. M. El-Tamimi, "An indicator system for evaluating the development of land-sea coordination systems: A case study of Lianyungang port," *Ecol. Indic.*, vol. 98, pp. 112–120, Mar. 2019.
- [49] Y. Lv, Y. Chen, X. Zhang, Y. Duan, and N. Li, "Social media based transportation research: the state of the work and the networking," *IEEE/CAA J. Autom. Sinica*, vol. 4, no. 1, pp. 19–26, Jan. 2017.



Cong Wang received the B.S. degree in automation and the M.S. degree in mathematics from Hohai University, Nanjing, China, in 2014 and 2017, respectively. He is currently pursuing the Ph.D. degree in mechatronic engineering, Xidian University, Xi'an, China.

He was a Visiting Ph.D. Student with the Department of Electrical and Computer Engineering, University of Alberta, Edmonton, AB, Canada. He is currently a Research Assistant at the School of Computer Science and Engineering, Nanyang Technological University, Singapore. His current research interests include wavelet analysis and its applications, granular computing, and pattern recognition and image processing.



Witold Pedrycz (M'88-SM'90-F'99) received the M.Sc., Ph.D., and D.Sc., degrees from the Silesian University of Technology, Gliwice, Poland.

He is a Professor and the Canada Research Chair in Computational Intelligence with the Department of Electrical and Computer Engineering, University of Alberta, Edmonton, AB, Canada. He is currently with the School of Electro-Mechanical Engineering, Xidian University, Xi'an 710071, China, and the Faculty of Engineering, King Abdulaziz University, Jeddah 21589, Saudi Arabia. He is also with the Systems Research Institute of the Polish Academy of Sciences, Warsaw, Poland. He is a foreign member of the Polish academy of Sciences. He has authored 15 research monographs covering various aspects of computational intelligence, data mining, and software engineering. His current research interests include computational intelligence, fuzzy modeling, and granular computing, knowledge discovery and data mining, fuzzy control, pattern recognition, knowledge-based neural networks, relational computing, and software engineering. He has published numerous papers in the above areas.

Dr. Pedrycz was a recipient of the IEEE Canada Computer Engineering Medal, the Cajastur Prize for Soft Computing from the European Centre for Soft Computing, the Killam Prize, and the Fuzzy Pioneer Award from the IEEE Computational Intelligence Society. He is a fellow of the Royal Society of Canada.



MengChu Zhou (S'88-M'90-SM'93-F'03) joined New Jersey Institute of Technology (NJIT), Newark, NJ in 1990, and is now a Distinguished Professor of Electrical and Computer Engineering. His research interests are in Petri nets, intelligent automation, Internet of Things, big data, web services, and intelligent transportation.

He has over 800 publications including 12 books, 500+ journal papers (400+ in IEEE TRANSACTIONS), 12 patents and 29 book-chapters. He is a Fellow of International Federation of Automatic Control (IFAC), American Association for the Advancement of Science (AAAS) and Chinese Association of Automation (CAA).



ZhiWu Li (M'06-SM'07-F'16) joined Xidian University in 1992. He is currently with the Institute of Systems Engineering, Macau University of Science and Technology, Macau, China. He was a Visiting Professor with the University of Toronto, Toronto, ON, Canada, the Technion-Israel Institute of Technology, Haifa, Israel, the Martin-Luther University of Halle-Wittenberg, Halle, Germany, Conservatoire National des Arts et Métiers, Paris, France, and Melikşah Üniversitesi, Kayseri, Turkey. His current research interests include Petri net theory and application, supervisory control of discrete-event systems, workflow modeling and analysis, system reconfiguration, game theory, and data and process mining.